

Geochemistry, Geophysics, Geosystems

RESEARCH ARTICLE

10.1029/2021GC009754

Key Points:

- Seawater collected offshore of a lava ocean entry zone in Hawaii had elevated particle, chlorophyll, nutrient, and iron concentrations
- Precipitation of iron oxyhydroxide in this volcanic fertilization event led to extensive scavenging of dissolved phosphate
- Laboratory experiments yielded estimates for phosphate partitioning and diffusive exchange into iron oxyhydroxide

Supporting Information:

Supporting Information may be found in the online version of this article.

Correspondence to:

R. K. Foreman,
rforeman@hawaii.edu

Citation:

Foreman, R. K., Björkman, K. M., Funkey, C. P., Hawco, N. J., Wilson, S. T., Rohrer, T., et al. (2021). Phosphate scavenging during lava-seawater interaction offshore of Kilauea volcano, Hawaii. *Geochemistry, Geophysics, Geosystems*, 22, e2021GC009754. <https://doi.org/10.1029/2021GC009754>

Received 3 MAR 2021

Accepted 2 JUN 2021

© 2021. The Authors.

This is an open access article under the terms of the [Creative Commons Attribution-NonCommercial License](#), which permits use, distribution and reproduction in any medium, provided the original work is properly cited and is not used for commercial purposes.

Phosphate Scavenging During Lava-Seawater Interaction Offshore of Kilauea Volcano, Hawaii

Rhea K. Foreman¹ , Karin M. Björkman¹ , Carolina P. Funkey¹ , Nicholas J. Hawco² , Samuel T. Wilson¹ , Tully Rohrer¹ , Angélique E. White¹ , Seth G. John³ , and David M. Karl¹ 

¹Daniel K. Inouye Center for Microbial Oceanography: Research and Education, Department of Oceanography, School of Ocean and Earth Science and Technology, University of Hawaii at Mānoa, Honolulu, HI, USA, ²Department of Oceanography, School of Ocean and Earth Science and Technology, University of Hawaii at Mānoa, Honolulu, HI, USA, ³Department of Earth Sciences, University of Southern California, Los Angeles, CA, USA

Abstract The 2018, subaerial eruption of Kilauea volcano, Hawaii, resulted in a 5-km-long stretch of coastline that actively drained lava into the ocean. Nutrients were added to the surrounding ocean through the dissolution of basaltic rock and thermal upwelling of deep water, thereby fueling a large phytoplankton bloom. Lava-impacted, surface seawater had high suspended particle loads, and concentrations of chlorophyll, silicic acid, phosphate (P_i), nitrate, and iron that were elevated up to 12, 36, 5, 960, and 1,400 times, respectively, above the background oligotrophic levels. Widespread precipitation of iron oxyhydroxides (Fe_{ox}) led to extensive scavenging of the dissolved P_i pool, similar to what occurs along mid-ocean ridge hydrothermal systems. This scavenging transformed a “fertilization” event into a P_i sink near the coast of the ocean entry; however, nutrient data from outside the bloom suggest that P_i could also desorb from the Fe_{ox} as it is dispersed into the open ocean. From lava quench experiments, we estimate that the hydration state of the Fe_{ox} precipitate (H_2O/Fe) was 5.2–5.7, and that the equilibrium partition coefficient of P_i into Fe_{ox} (solid/liquid) was 10^6 . In addition, $^{33}P_i$ radiotracer incubations were used to differentiate between biotic and abiotic uptake of P_i at Kilauea’s ocean entry. These findings are important for understanding modern-day volcanic fertilization events, modeling nutrient dynamics during major events in Earth history (such as oxygenation of the atmosphere and the formation of large igneous provinces), and predicting the marine response to greater continental weathering in a warming climate.

1. Introduction

Phosphorus (P) is an obligate requirement for life on Earth and is essential for nucleic acids, membranes, and energy stores within all living cells. The P budget and its distribution in the oceans have an enormous impact on ecosystem dynamics and community compositions, and P is often the nutrient that limits primary productivity (Karl, 2002; Sohm et al., 2011; Tyrrell, 1999). Therefore, knowing the abiotic controls on the sources and sinks of marine P, especially dissolved phosphate (PO_4^{3-} , hereafter P_i), is crucial for understanding the biogeochemistry of both modern and ancient oceans.

Volcanically driven nutrient fertilization is a potentially important source of P_i , as well as iron (Fe), silicon (Si), and sometimes nitrogen (N), to the surface ocean (Achterberg et al., 2013; Duggen et al., 2010; González-Vega et al., 2020; Hamme et al., 2010; Karl et al., 1988; Resing & Sansone, 2002; Wilson et al., 2019). However, there are few direct biogeochemical observations from the field due to the unpredictable timing and often remote locations of volcanic eruptions. Here, we present data from a rare opportunity that allowed us to sample the surface ocean offshore of Kilauea volcano, Hawaii, during active lava-seawater interaction. Field data are complimented with laboratory-based lava quench experiments, and particular attention is given to the biogeochemistry of P_i .

Kilauea volcano, on the island of Hawai‘i, is one of the most active volcanoes in the world, displaying a nearly constant effusion of lava and gases throughout all of recorded history. In 2018, Kilauea’s eruptive conditions changed dramatically with a voluminous fissure eruption along the lower East Rift Zone and synchronous collapse of the summit caldera (Neal et al., 2019). Eruptive fissures (24 in total) began opening May 3, 2018, and by May 28, 2018, activity became focused at fissure 8, recently named Ahu‘aila‘au. Effusion rates of 50–200 m^3/s from Ahu‘aila‘au fed highly channelized lava flows that reached the south-

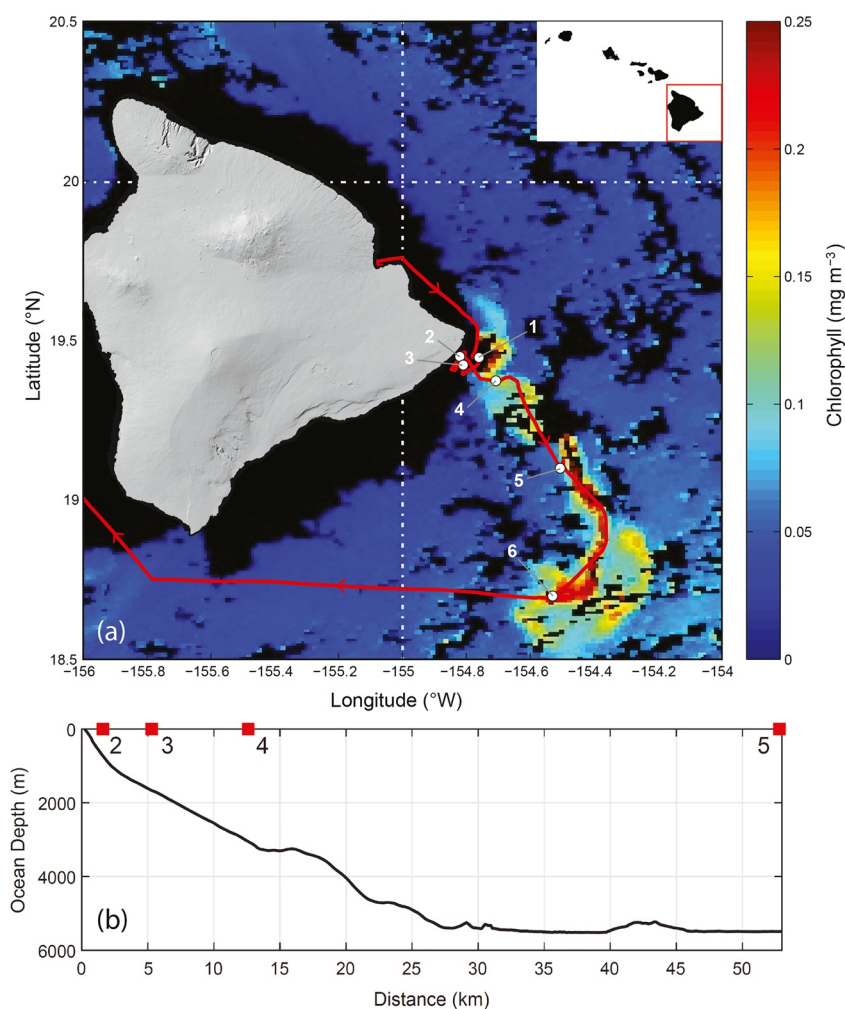


Figure 1. (a) MODIS satellite chlorophyll from July 10, 2018 with cruise ship track in red and station numbers in white. The hillshade image of Hawai'i Island was created using U.S. Geological Survey 10 m Digital Elevation Models and is available through the State of Hawaii. Panel (b) shows the bathymetric profile along a straight line from the coast to Station 5 and is plotted using the GMRT Grid (version 3.7) available through GeoMapApp.

eastern coastline on June 3, 2018, filled in Kapoho Bay, and created 3.5 km² of new land area by the end of the eruption in August (Neal et al., 2019). Submarine lava flows reached water depths of at least 750 m along the front of the new lava delta (Soule et al., 2021) and drove frequent offshore hydrovolcanic explosions of steam, seawater, and volcanoclastic debris (like those described in Mattox & Mangan, 1997; Figure S1).

Three days after lava began entering the ocean, satellite observations of the upper water column revealed high levels of chlorophyll along flow lines leading away from the ocean entry site, into waters that are normally oligotrophic with very low primary productivity (Figure 1). A rapid-response oceanographic expedition was conducted during July 13–15, 2018 to investigate the active phytoplankton bloom and its biogeochemical origins. Details of the interdisciplinary expedition were reported by Wilson et al. (2019). In summary, they found that elevated levels of chlorophyll (up to 0.6 μg/L from a background of 0.05 μg/L) were coincident with elevated trace metals and rare earth metals in ratios that reflect the composition of Kilauean basalt, together with elevated inorganic nutrients. Wilson et al. (2019) concluded that the diatom-rich phytoplankton bloom depended on two linked sources of nutrient fertilization to the euphotic zone: (1) submarine dissolution of basaltic glass as the main contributor of Fe, Si, and P_i to the seawater, and (2) upwelling of lava-warmed, nutrient-rich deep waters as the main (and probably only) source of nitrate, as well as a secondary source for Si and P_i.

Complicating the nutrient dynamics in this setting is the well-known observation that P_i is removed from solution through adsorption onto volcanogenic iron oxyhydroxides (Fe_{ox} ; Berner, 1973). Such Fe_{ox} form by spontaneous precipitation when lava-derived, soluble Fe(II) is oxidized to insoluble Fe(III) on a timescale of minutes (González et al., 2010; Santana-González et al., 2017). Indeed, Hawco et al. (2020) report that <1% of the lava-derived Fe remained in solution within the 2018 phytoplankton bloom, thereby providing a potent sink for P_i . Here, we expand on the studies from Wilson et al. (2019) and Hawco et al. (2020) to gain a deeper understanding of this important aspect of the marine P cycle. We present new field and experimental data on: particle counts and size distributions; particulate Si, Fe, and P concentrations; dissolved nutrient concentrations; and $^{33}P_i$ radiotracer incubations. In combination, these data allow us to differentiate between biotic and abiotic uptake of P_i offshore of Kilauea, estimate the hydration state of Fe_{ox} and the partition coefficient of P_i into Fe_{ox} , and evaluate the overall mass balance of nutrients within and outside of the phytoplankton bloom.

2. Methods

2.1. Field Observations and Sampling

Samples were collected during the Life Aquatic in the Volcanic Aftermath (LAVA) expedition on the *R/V Ka'imikai-O-Kanaloa* (cruise ID: KOK1806) from July 13 to 15, 2018, during peak discharge of lava into the ocean. Lava was entering the ocean along ~5 km of coastline, boiling seawater, and generating an acidic steam cloud (termed a laze plume, derived from “lava haze”) that was advected inland due to the prevailing wind direction from northeast to southwest (Figures S2–S5). Seawater immediately offshore was discolored to a greenish brown and roiling due to hydrovolcanic explosions (Figures S1, S6 and S7). Due to safety concerns, the closest sampling station was ~1 km offshore, outside of the most turbulent waters.

The cruise path targeted the plume of high satellite-derived chlorophyll leading away from the coastline of the lava ocean entry site (Figure 1). Seawater was sampled in three ways: through the ship's underway seawater sampling system (intake depth of ~6 m); using a Niskin® bottle rosette (24 × 10 L) in order to obtain depth profiles (5, 25, 45, 75, 100, and 125 m) at six stations; and through a trace-metal-clean, tow-fish pumping apparatus that was deployed when we were underway between stations (beginning after Station 3) and sampled at a depth of ~1–3 m (see Hawco et al., 2020 for details on the tow-fish assembly and operation). The shipboard underway system provided continuous observations of chlorophyll and particle size distributions as well as some discrete nutrient samples. From depth profiles, we sampled for suspended particle loads (mg/L) and nutrient concentrations, and obtained source water for $^{33}P_i$ incubations. From the tow-fish, we obtained discrete samples for nutrient and Fe analyses. Note that some tow-fish data and underway chlorophyll were originally reported in Wilson et al. (2019), and an extensive data set and discussion of trace metal and rare earth element data obtained from the tow-fish sampler was provided by Hawco et al. (2020).

Station 1 was outside of the lava-impacted plume and was chosen in order to provide a background reading of the near-coastal water chemistry. Station 2 was closest to the lava entry (~1 km offshore) and at an ocean depth of nearly 1,000 m (Figure 1b). Bathymetric evidence of new submarine lava flows was observed to a depth of 750 m (Soule et al., 2021), although it is possible that some changes in bathymetry represented mass wasting from flows that were emplaced at more shallow depths (Sansone & Smith, 2006). In either case, Station 2 and beyond recorded the chemistry of water that was advected both vertically (by thermal upwelling off of the hot submarine lava flows) and horizontally (by surface currents; Wilson et al., 2019).

2.2. Synthetic Ocean Entry

A laboratory-based experiment simulating lava-seawater interaction was conducted in order to: (1) generate Fe_{ox} particles in situ; (2) study the P_i and Fe dynamics in a contained system (open to gas exchange but not water or particles); and (3) eliminate biological processes. We used natural basaltic rock collected from the 1859 lava flow from Mauna Loa, north of Kailua-Kona on the island of Hawai'i, because there was very limited accessibility to the new 2018 flow field. The rock sample was cleaned in deionized water and dried at 150°C before use. The major element composition of the basalt was determined by X-ray fluorescence spectrometry at the Peter Hooper GeoAnalytical Lab at Washington State University, and found to be very similar to the lava from Ahu'aila'au (Table 1; Gansecki et al., 2019). Molten lava was formed by melting

Table 1
Major Element Compositions of Basalt

	Mauna Loa 1859 flow	Ahu'aïla'au 2018 eruption ^a
Oxide (wt%)		
SiO ₂	52.00	50.93
TiO ₂	2.30	2.46
Al ₂ O ₃	13.62	13.33
FeO	11.23	11.25
MnO	0.17	0.17
MgO	7.27	8.19
CaO	10.23	10.67
Na ₂ O	2.44	2.30
K ₂ O	0.47	0.46
P ₂ O ₅	0.27	0.23
Total	100.00	100.00
Molar ratios		
Si/P	226	260
Si/Fe	5.54	6.02
Fe/P	40.8	43.2

^aAhu'aïla'au composition from Gansecki et al. (2019).

the basalt to 1200°C–1250°C in a silicon carbide crucible in collaboration with the University of Hawaii at Mānoa Art Department. A synthetic ocean entry was made in quadruplicate by quenching 0.6–1.9 kg of melt into 10 L stainless steel beakers filled with 4–6 L of 0.2 μm-filtered surface seawater collected from Station ALOHA, 100 km north of Oahu (Karl & Lukas, 1996). In each of the four beakers, the seawater boiled, and in one beaker (Beaker A) the rock-to-water ratio (0.5 kg/L) was high enough that a laze plume was generated. Contamination of P_i was monitored using a control beaker of seawater without lava addition, and found to be inconsequential. About 5 min after the lava was quenched, seawater samples were taken for Si and P_i analyses. The basaltic glass was left in the beaker of seawater during subsequent sampling over the next day. The quench water was then decanted through a 200 μm mesh (to remove basaltic glass shards) and stored at 4°C for subsequent work, including P_i partitioning, particle abundances and size distributions, and total Fe analyses. Before any other analyses of the quench water, the samples were removed from the refrigerator and allowed to equilibrate at room temperature for two weeks.

2.3. Characterization of Particles

Dry weights (i.e., suspended particle load in units of mg/L) of seawater samples from each field station were determined in duplicate using 47 mm Whatman GF/F glass fiber filters (nominal retention size of 0.7 μm) after they were pre-combusted at 450°C for 5 h, cooled, and weighed. Filtered seawater volume was 2 L for all samples. After filtering,

filters were rinsed twice with deionized water to remove sea salts before storing at –20°C for the duration of the cruise. Dry weights were determined after drying at 60°C for 48 h. Ash-free dry weights (i.e., the fraction of combustible particles) were determined by difference in weight after combustion at 450°C for 5 h. Dry weights of samples from the synthetic ocean entry experiments were determined in triplicate by filtering 25–50 mL of sample onto pre-weighed 25 mm Whatman Nuclepore filters with 0.2 μm pore size instead of the 47 mm GF/F filters used for field samples in order to match the filters used for the ³³P_i uptake experiment (see below).

Particle size distributions in both the field and experimental samples were determined with a Laser In-Situ Scattering and Transmissometry instrument (Sequoia LISST-100X). Field samples were measured using a continuous, flow-through sample chamber plumbed to the ship's underway seawater sampling system. For the first 10 minutes of every hour, for the duration of the cruise, the instrument sampled filtered seawater (<0.2 μm); these background values were subtracted from the data before inversion. The experimental samples were scanned by the LISST as discrete aliquots in a closed, gently stirred sample chamber, and averaged over one minute at a sampling rate of 10 Hz. Lab samples were corrected to remove background scattering of deionized water. All data processing was done in MATLAB using manufacturer-supplied code for the background scattering correction (getscat.m), scattering inversion (invert.p using 15 iterations), and laser power and concentration corrections (vdcorr.m), as described in White et al. (2015). The particle volume (μL/L) in each size bin was converted to particle concentration (#/L) assuming a spherical geometry; the total particle concentration was the sum of particles in log-spaced bins spanning a median diameter of 1.25–100 μm. Particle size distributions were normalized to bin width (which varies) in order to standardize counts into 1 μm sized increments.

2.4. Dissolved Nutrients

From the field expedition, all seawater samples destined for nutrient analyses were collected into acid-cleaned polypropylene bottles or trace-metal-free 50 mL centrifuge tubes (VWR), and stored at –20°C until analysis (Dore et al., 1996). Nutrient samples from the Niskin® bottles (Station 1–6, depth profiles)

were pre-screened through a 50 μm mesh and those from the tow-fish were pre-filtered using a 0.2 μm polyethersulfone Acropak 1500 capsule filter. Nutrient samples from the synthetic ocean entry experiment were centrifuged (1000 \times g for 15 min) before analysis to remove particles.

Nitrate plus nitrite ($\text{NO}_3^- + \text{NO}_2^-$; hereafter N + N) concentrations were determined following Strickland and Parsons (1972), adapted for segmented flow on a SEAL AutoAnalyzer III (AA3) with a high resolution detector. This method has a quantification limit of ~ 50 nM N + N, and an accuracy of $\pm 1\%$ as determined by daily measurements of the Wako CSK standard solution at 5.0 μM NO_3^- (Wako #036-10191). Samples with N + N of < 100 nM were analyzed using the chemiluminescent method of Foreman et al. (2016), which has a detection limit of 1 nM. P_i concentrations were determined on the AA3 following Murphy and Riley (1962), with a quantification limit of ~ 30 nM and an accuracy of 2% as determined by daily measurements of the Wako CSK standard solution at 0.5 μM P_i (Wako #034-10011). Silicic acid ($\text{Si}[\text{OH}]_4$, hereafter Si) concentrations were determined using the silicomolybdic acid method described in Koroleff (1983), with a quantification limit of ~ 40 nM and an average accuracy of 3% as determined by daily measurements of the Wako CSK standard solution at 5.0 μM Si (Wako #039-10061). Ammonium analyses were made using the fluorometric method of Holmes et al. (1999; high sensitivity protocol) with a quantification limit of 5 nM.

2.5. Particulate Iron, Phosphate, and Silica

Total dissolvable iron (tdFe) in surface waters of the phytoplankton bloom was determined using unfiltered seawater from the trace-metal-clean tow-fish sampling system. Samples were acidified to a pH of 1.8 with 12 N HCl, and left to equilibrate for > 1 month before being analyzed by inductively coupled plasma mass spectrometry (ICP-MS) on an Element 2 (Thermo; for analytical details see Hawco et al., 2020). Unfiltered seawater samples taken from the synthetic ocean entry experiments were diluted 100-fold with 0.1 N nitric acid for dissolution (because of high Fe content) and analyzed directly by ICP-MS.

Particulate phosphate (PPO_4) was determined in two ways. For experimental samples, total dissolvable phosphate (tdP_i) was measured in the tdFe splits, then PPO_4 was calculated by subtracting background P_i from tdP_i; with propagation of analytical error, precision of this difference calculation is estimated to be $\pm 3\%$. Particulate organic P was assumed to be negligible in the lava quench experiments. Field samples had an order of magnitude lower PPO_4 concentration and required pre-concentration for analysis. PPO_4 from Stations 1–6 was quantified by filtering 0.5 L onto combusted, HCl-cleaned GF/F filters. The filters were placed into combusted, HCl-cleaned borosilicate tubes and stored at -20°C until analyzed. For analysis, the PPO_4 filters were ashed at 450°C for 6 h to oxidize organic P, then leached in 10 mL of 0.15 N HCl for 1 h, before being mixed by vortex and centrifuged at 1000 \times g for 15 min to remove filter debris. A 5 mL subsample was removed and analyzed for P_i (Murphy and Riley, 1962) at a detection wavelength of 880 nm on a Beckman DU-640 spectrophotometer. We were unable to analyze PPO_4 concentrations in tow-fish samples due to low concentrations and small sample volumes (40 mL).

Particulate Si (PSi) for the upper 45 m of Stations 1–6 was collected by filtering 0.5 L of seawater onto a 0.8 μm polycarbonate (PC) filter, followed by a time course leaching of the filter in a 0.1 M sodium carbonate solution at 85°C (DeMaster, 1981), which allows for the distinction between biogenic Si (opal from diatoms) and lithogenic Si (basalt fragments) due to differences in their dissolution kinetics. Digested samples were analyzed for dissolved Si concentrations using the chemistry of Koroleff (1983) with detection at a wavelength of 810 nm on a Beckman DU-640 spectrophotometer.

2.6. $^{33}\text{P}_i$ Uptake Experiments

To evaluate the uptake rate of P_i into field particles, by the sum of both biotic and abiotic processes, surface seawater from all 6 stations (5 m deep, sampled with the Niskin® rosette) was collected into HCl-washed, sample-rinsed, 4 L PC bottles and incubated in on-deck incubators that were cooled with flowing surface seawater and shaded to 50% surface irradiance using blue shielding (Arkema #2069). Untreated seawater samples were kept in the incubator for 0 to 15 h before subsampling for rate measurement in order to start all radiotracer experiments at dawn. At the start of each experiment, triplicate 75 mL PC bottles were spiked with $^{33}\text{P}_i$ (^{33}P -orthophosphoric acid; PerkinElmer #NEZ0800) to a final activity of 555 kBq/L and returned to

Table 2
Chemical Parameters for Seawater and Particles in Lava Quench Experiments

	Experimental beaker			
	A	B	C	D
Lava added (kg)	1.91	0.64	0.71	1.30
Seawater volume, initial (L)	4	4	4	6
Rock/Water ratio (kg/kg)	0.47	0.16	0.17	0.21
Seawater, recovered (kg)	1.786	2.457	2.673	n.d.
Final dissolved Si (μM)	121.6	39.1	41.2	43.4
Final dissolved P_i (μM)	0.044	0.054	0.036	0.068
td P_i (μM)	0.791	0.220	0.314	0.199
tdFe (μM)	69.8	17.3	33.2	15.2
Particle abundance (mg/L)	13.0	3.4	5.6	3.1
tdFe/(td P_i - P_i at $t = 0$) ^a	91	103	115	96
Dissolved Si/(td P_i - P_i at $t = 0$) ^a	162	232	145	325
Log K_d of P_i (particles/water)	6.1	6.0	6.2	5.8

^aThese ratios are calculated after correcting total dissolvable P_i (td P_i) for background P_i in the starting surface seawater (0.03 μM), before lava addition.
n.d., not determined.

the incubator. Samples for P_i and PPO_4 were taken from the 4 L bottles at the start of the tracer incubation experiments before $^{33}\text{P}_i$ addition. P_i pool turnover times and P_i uptake rates were determined by time course sampling of the $^{33}\text{P}_i$ incubations over 4 h. A subsample from each of the incubations was collected to quantify total radioactivity. At each time point, 10 mL from each of the incubations was filtered onto a 0.2 μm PC filter to measure $^{33}\text{P}_i$ uptake into particles. At the last time point, the incubations were also size fractionated using 10, 2, 0.6, and 0.2 μm PC filters. The filters and total radioactivity subsamples were placed into 7 mL plastic scintillation vials (Simport) with 4 mL of scintillation cocktail (Ultima-Gold LLT, PerkinElmer). Radioactivity was measured using a PerkinElmer 2100 liquid scintillation counter. The rate of uptake was determined from the slopes of the time course activities for each triplicate, and the P_i pool turnover time (TOT) was calculated as the total activity divided by the rate of uptake in days. The mean TOT ($n = 3$) was used to calculate the P_i uptake rate (nM/d) by dividing the measured P_i concentration by the TOT.

The magnitude of abiotic scavenging of P_i by lava-derived particles was evaluated through $^{33}\text{P}_i$ incubations of seawater obtained from the synthetic ocean entry experiment (quench water passed through 200 μm mesh to remove large glass shards but not Fe_{ox} particles). A subsample from experimental Beaker A (see Table 2) was used undiluted (100%) as well as diluted (20%) with 0.2 μm -filtered surface seawater from Station ALOHA in order to yield a similar Si concentration as measured at Station 2 of the LAVA expedition (25 μM ; 5 m depth). A control sample containing only the filtered surface seawater dilutant was also incubated with $^{33}\text{P}_i$ spike and used as a background correction for the 20% dilution. For each sample or control, triplicate incubations of 200 mL were placed into HCl-cleaned PC bottles and spiked with $^{33}\text{P}_i$ to a final activity of approximately 370 kBq/L. The incubations were subsampled for (1) total radioactivity in the whole water, (2) activity retained on a 0.2 μm PC filter, and (3) activity in the filtrate at 5, 20, and 60 min, and 2, 4, and 6 h, then 1, 2, and 5 days after the $^{33}\text{P}_i$ spike. Radioactivity was measured in the same way as field samples. An incubation of filtered, sterilized seawater showed undetectable loss of $^{33}\text{P}_i$ from the seawater and no change in total activity over time (corrected for decay using a half-life of 25.34 days), indicating that there was no loss of $^{33}\text{P}_i$ to the container surface. In addition, activity in the filter plus activity in the filtrate generally summed to within error of 100% of the total measured activity.

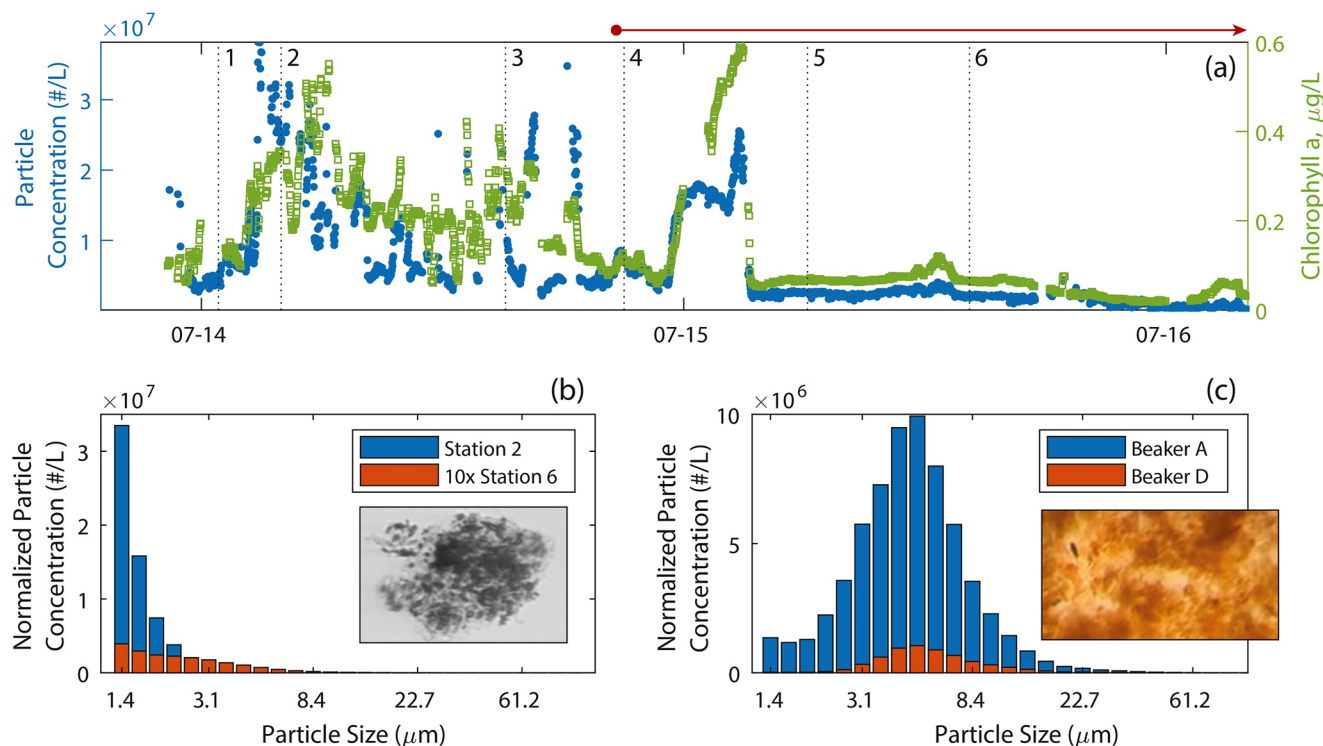


Figure 2. Particle counts from LISST and chlorophyll concentrations found in surface waters along the cruise track (a). The x-axis shows the date (mm-dd) in 2018 with ticks at the start of each new day (midnight); station locations are marked with vertical dotted lines and the horizontal red arrow indicates coverage from the tow-fish sampler. Particle size distributions from the field stations (b) and the synthetic ocean entry experiments (c) are shown for the samples with highest and lowest particles counts in each setting. Station 6 is displayed as 10 times actual counts in order to be visible. Inset microscopy images show particles from the field (b) and an experimental sample (c).

3. Results

3.1. Field Particles

All biogeochemical parameters that were monitored within the lava-impacted phytoplankton bloom showed a high degree of spatial heterogeneity. This is well represented in the trends of chlorophyll and particulate matter along the transect (Figure 2), especially from Stations 1–5. As chlorophyll varied between 0.05 and 0.6 $\mu\text{g/L}$, particle counts (from LISST) varied by more than 10-fold, with the two parameters displaying very tightly linked peaks and troughs that changed over timescales of minutes along the cruise track. Various patchy peaks occurred from just past Station 1 to mid-way to Station 4. Another broad, but smooth, peak occurred between Stations 4 and 5, which was sampled for metals and nutrients by the tow-fish sampler.

The particle size distribution (PSD) at Station 2, the closest station to the active lava entry, indicated a predominance of particles $<3 \mu\text{m}$ in diameter, similar to that observed distally at Station 6 (Figure 2b). Consistent PSDs and the correlation of particle abundance with chlorophyll concentration may lead one to conclude that most particles were phytoplankton cells. However, the proportion of combustible particles (i.e., % organic particles) decreases with increasing particle abundance. Figure 3 shows a range in dry weights of 0.4–3 mg/L for whole water samples taken from Stations 1–6 at depths of 5–125 m. Overall, there is a clear trend of increasing organic matter (mg/L) with increasing dry weight (mg/L) (Figure 3a), but the percentage of organic particles decreases from 70% at low particle loads to 20% at the highest particle loads (Figure 3b). Because the phytoplankton bloom was diatom-rich (*Skeletonema* sp. comprised 37% of the carbon biomass; Wilson et al., 2019), a component of the inorganic material was biogenic silica. Maximum concentrations of biogenic silica (1.1–2.4 $\mu\text{M SiO}_2$; see supporting information) were found at Station 2, coincident with some of the highest dry weights that are shown in Figure 3; however, this only amounts to 0.07–0.14 mg/L of the total dry weight (a 3%–7% correction) and does not explain the high inorganic particle load near the ocean entry. Furthermore, the slope of the regression in Figure 3a (at 0.2) is much too shallow

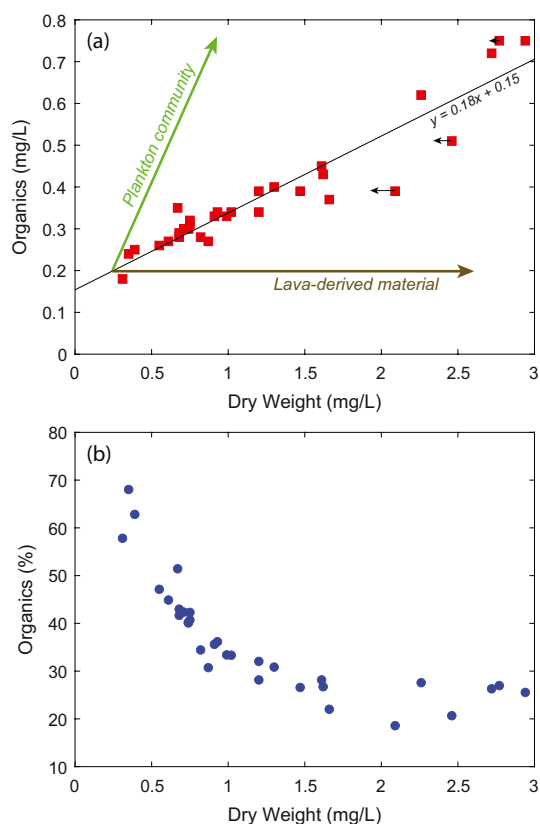


Figure 3. Organic matter (a) and % organic matter (b) plotted against total dry weight of field samples from Stations 1–6 at water depths of 5–125 m. Small black arrows on the samples in panel (a) indicate the change in dry weight upon correction for biogenic silica concentrations in the 3 samples with the highest P_{Si} concentrations. The green arrow in panel (a) shows the relationship between dry weight and organic matter that is expected from the planktonic community composition reported by Wilson et al. (2019). These trends are interpreted as mixing between background oligotrophic water and lava-impacted water that contains both increased biological activity and the rock-derived components that stimulated the bloom.

to represent the planktonic community composition in the lava-impacted bloom, which we estimate should be 0.8 based on the distribution of species reported in Wilson et al. (2019), assuming diatoms have a 1:1.5 relationship between organic mass and total mass (Huntley et al., 2015) and all other species that were present have a 1:1 relationship.

Multiple additional lines of evidence lead to the conclusion that the high inorganic particle loads were not of biological origin, and instead were dominated by Fe_{ox}. The dry weight filters were discolored to a reddish brown and microscopic investigation revealed many inorganic flocs of material. Hawco et al. (2020) reported that dissolved manganese (Mn) and total dissolvable Mn (tdMn) followed a 1:1 line (i.e., there was negligible particulate Mn), indicating that elevated trace metals in the bloom were derived from the dissolution of basalt and were not present as basaltic glass particles. However, they also show that dissolved Fe (<0.2 μm) was only ~1% of the tdFe, meaning 99% of the lava-derived Fe had reprecipitated as Fe_{ox}. Their significant correlation between Mn and tdFe, at a ratio consistent with basalt (~65), suggests that the precipitated Fe_{ox} particles largely stayed in suspension within their native water mass in the most lava-impacted waters.

3.2. Field Nutrients and Iron Concentrations

All nutrient data are provided in the supporting information. Figure 4 shows concentrations of tdFe, Si, N + N, and P_i from tow-fish underway sampling of surface waters along the cruise transect, which began just ahead of Station 4. Tow-fish sampling was paused during on-station work, so some sections of the particle and chlorophyll time series shown in Figure 2 do not have corresponding tow-fish nutrient data. Background concentrations in the oligotrophic surface waters surrounding Hawaii are: tdFe = 0.001 μM; Si = 1 μM; N + N = 0.005 μM; and P_i = 0.07 μM (Boyle et al., 2005; Karl et al., 2001). A distinct peak in tdFe, Si, and N + N occurred between Stations 4 and 5, with increases of roughly 1400, 14, and 200 times, respectively, over background. An increase in P_i is noticeably absent from the nutrient peak; instead, P_i concentrations were close to background levels up to Station 5 and then displayed a long broad arc of slightly elevated values to Station 6 and beyond, where tdFe and Si had roughly returned to background concentrations and no other indicators of lava input were present (Hawco et al., 2020). A small peak in N + N, up to 0.13 μM or 26 times over background, was found near Station 6.

Increased spatial coverage of nutrient concentrations in the bloom was obtained from depth profiles at the 6 stations and some analyses of Si and P_i concentrations in samples from the ship's underway sampling system in the vicinity of Stations 2 and 3. The most lava-enriched waters were found at Station 2 (5–45 m) and its surrounding area, with Si up to 36 μM, P_i up to 0.38 μM, and N + N of almost 5 μM (36, 5, and 960 times over background, respectively; Figure 5). Ammonium concentrations analyzed from the profile samples were slightly anomalous at Station 2, but still at very low concentrations (30–54 nM) compared to a range of 1–44 nM from all the other profiles (see supporting information). Low ammonium suggests that hydrothermal venting was not a significant source of nutrient addition to the lava-impacted waters (Karl et al., 1988).

PPO₄ concentrations were very high (0.11–0.16 μM) for the 5–45 m deep samples from Station 2 that also had the highest dissolved nutrient loads and highest particulate Si. All other profile samples together ($n = 33$) had an average PPO₄ concentration of $0.023 \pm 0.007 \mu\text{M}$ (1σ). The rate of P_i uptake into the particulate pool, as determined by the ³³P_i radiotracer incubations of surface seawater (5 m only), also varied significantly (Figure 6a). Stations 5 and 6 (farthest from the coast) have particulate P_i uptake rates of 3 nM/day, which are typical for biological uptake in the oligotrophic North Pacific Subtropical Gyre (Björkman

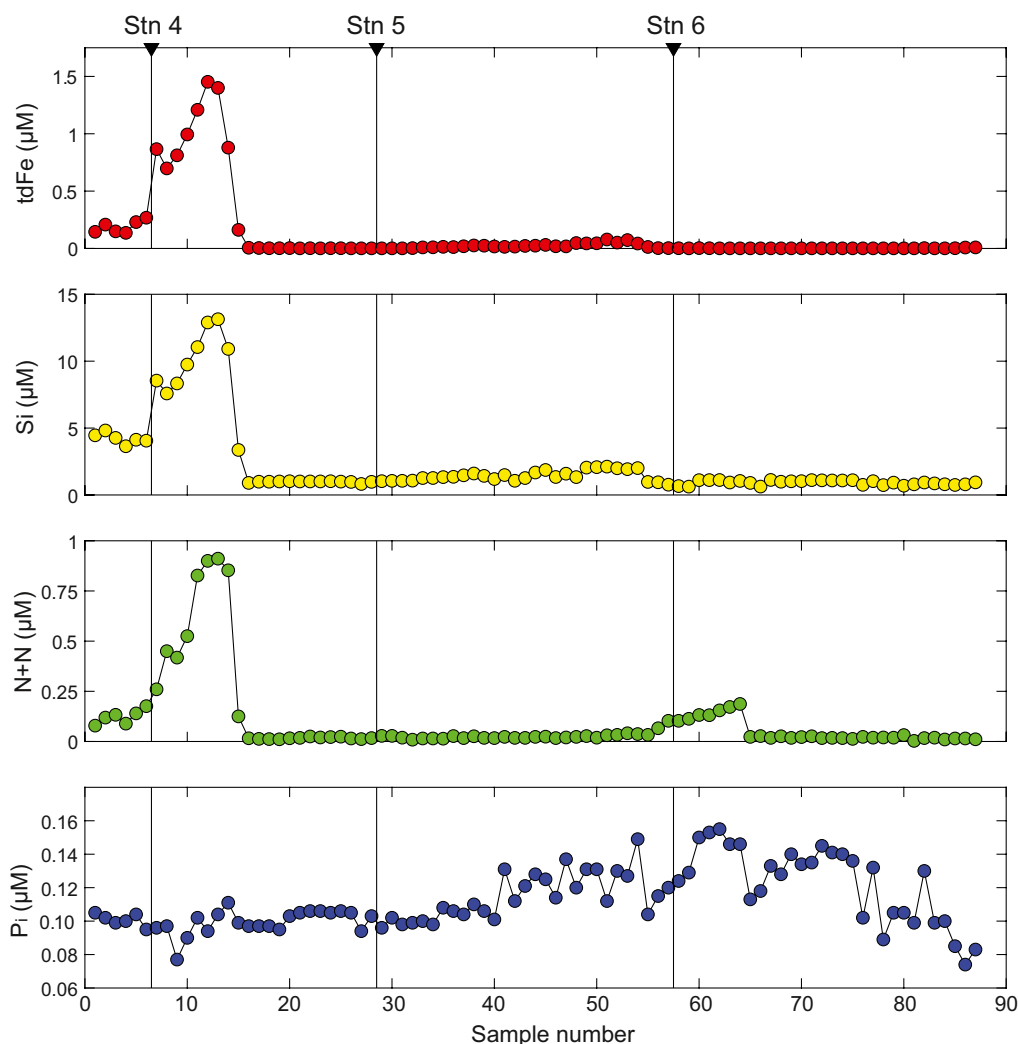


Figure 4. Total dissolvable Fe and macronutrient concentrations in underway tow-fish samples. Acquisition of tow-fish samples began after Station 3. Locations for Stations 4, 5, and 6 are marked with vertical lines.

et al., 2012; 2018). Rates at stations 1–4 are much higher, ranging from 10 nM/day up to a highly anomalous maximum of 70 nM/day at Station 2. Applying ^{14}C -based primary productivity estimates and bulk particulate carbon measurements from Wilson et al. (2019), the molar C:P uptake ratio at Station 2 was 45 and the bulk particulate C:P ratio was 21–28, both much lower than the Redfield ratio of 106 and indicative of excess particulate P. Size-fractionated ^{33}P samples indicated that the excess P_i was especially enhanced in the 0.6–10 μm size fractions (Figure 6b), which likely contained abundant Fe_{ox} flocs, as seen in the laboratory-based abiotic uptake experiment (see Section 3.4).

3.3. Synthetic Ocean Entry

The starting seawater for the laboratory-based, lava quench experiments had P_i and Si concentrations of 0.03 and 0.7 μM , respectively. After lava was poured into the beakers of seawater, both P_i and Si increased throughout the next few hours as the rock cooled (and continued to equilibrate) in the seawater. By the next morning, when we separated rock and water (using 200 μm mesh), the dissolved Si concentrations had stabilized and remained constant for the duration of our observations. Final Si concentrations for the four beakers ranged from 38 to 122 μM (Table 2). On the other hand, P_i concentrations showed precipitous drops after the initial increases, to the point that in Beaker A (with the highest Si) the dissolved Si/ P_i molar ratio equilibrated to 2750 although the rock ratio is 226 (Table 1). Final, dissolved P_i concentrations

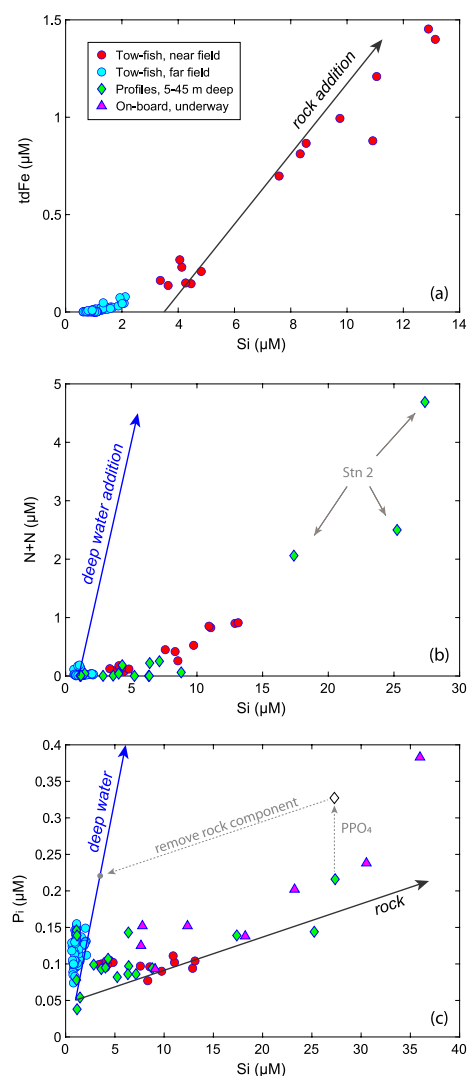


Figure 5. Covariation plots of Si with (a) tdFe, (b) N + N, and (c) P_i for field samples, overlaid with mixing trajectories for the dissolution of basalt and addition of deep water. Addition of deep water in (a) and rock dissolution in (b) are horizontal, only changing Si concentrations. Note that the range of the Si concentrations changes in each panel. Panel (b) identifies the most lava-enriched samples from Station 2. The gray, dotted arrows and white diamond in panel (c) are a graphical representation of the mass balance calculation discussed in Section 5.4.

(Table 2) were of similar concentration as the starting seawater and remained stable (within analytical precision) for the duration of our observations (>1 year). One uncertainty is whether the early decrease in P_i was due to co-precipitation with Fe_{ox} or adsorption onto already formed Fe_{ox} particles. We do not believe that biological activity played a role in the decrease of dissolved P_i for the following reasons: (1) the initial seawater had been filtered to $0.2 \mu\text{m}$, (2) the seawater boiled during the lava quenches, (3) P_i concentrations stabilized after the initial, rapid decrease, and (4) storage in the dark at 4°C inhibits biological activity.

Particle loads in the four beakers ranged from 3 to 13 mg/L and contained $0.13\text{--}0.75 \mu\text{M}$ PPO_4 and $15\text{--}70 \mu\text{M}$ tdFe (Figure 7; note that the highest tdFe found in the field was $1.4 \mu\text{M}$). The synthesized particles are generally larger than those observed in the field, with a peak at $5\text{--}7 \mu\text{m}$, but visually they are very similar, appearing as reddish brown flocs with feathery edges that aggregate as they settle (Figure 2). Therefore, we expect experimental particles to behave very similarly to field particles with respect to partitioning of P_i . Basaltic glass shards were rarely observed in the particulate fraction via microscopy, confirming that screening the seawater through $200 \mu\text{m}$ mesh was successful at removing undissolved rock fragments and isolating the Fe_{ox} flocs. The experimental particles contain $0.042\text{--}0.058 \mu\text{mol}$ P_i/mg , which match field particles from Station 2 ($5\text{--}45 \text{ m}$) that have an average of $0.055 \mu\text{mol}$ P_i/mg . When a subsample of each quench experiment was spiked with an additional $3 \mu\text{M}$ P_i , there was additional uptake by the particles (not shown), indicating that the Fe_{ox} particles were undersaturated with respect to P_i .

The ratio of tdFe to total P_i (corrected for background seawater concentrations) ranged from 91 to 115 in the quench water, but the rock ratio of Fe/P is 41 (Table 1). It seems likely that the system's high Fe/ P_i results from additional contribution of Fe from the stainless-steel beakers used for the experiment, as rust spots were observed in the beakers after use. However, it is also possible that not all of the rock-derived P appears as P_i in solution. If some portion of the rock-derived P was in solution as pyrophosphate or polyphosphate (Yamagata et al., 1991), it would not have been detected with the colorimetric analysis, and led to an apparent excess of Fe.

3.4. $^{33}\text{P}_i$ Uptake Experiment

Results from the $^{33}\text{P}_i$ radiotracer experiment using quench water from Beaker A at full strength (100%) and at a 5-fold dilution (to match the Si concentration at field Station 2) are shown in Figure 8. Because the quench water and Fe_{ox} particles had equilibrated for months, and the addition of $^{33}\text{P}_i$ changes the P_i concentration by only $\sim 1 \text{ pM}$, the results for the 100% quench water should be interpreted as self-diffusion, defined as diffusive exchange in the absence of a gradient in chemical potential (i.e., “random-walk” of P in and out of P sites, and not uptake due to disequilibrium in concentration). The 20% dilution was made right before the $^{33}\text{P}_i$ incubation, so there may have been some disequilibrium in concentration introduced, but it was likely minimal since the surface seawater diluent did contain a very similar dissolved P_i concentration ($0.035 \mu\text{M}$ compared to $0.044 \mu\text{M}$ in Beaker A).

For both incubations, a significant portion of $^{33}\text{P}_i$ was exchanged rapidly within the first 6 h, followed by a slower exchange. After 5 days, particles had adsorbed 62% and 23% of the $^{33}\text{P}_i$ spike in the 100% and 20% waters, respectively, and had yet to show a plateau that would indicate isotopic equilibrium had been reached. These observations are consistent with there being two established modes of adsorption/desorption of P_i into Fe_{ox} : a rapid exchange of anions adsorbed onto the particle surfaces and a slower exchange of anions

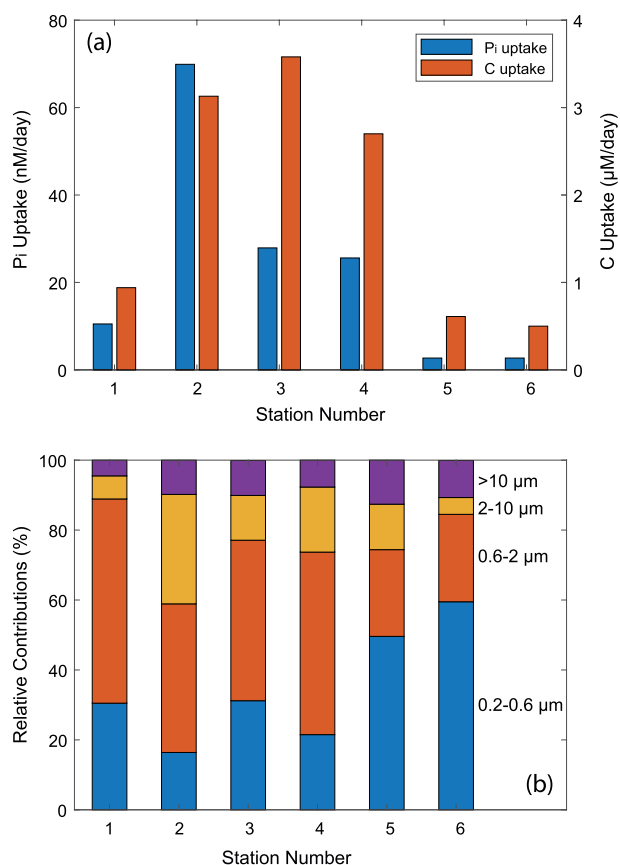


Figure 6. Inorganic bicarbonate uptake rates (Wilson et al., 2019) and P_i uptake rates (this study) for Stations 1–6 at 5 m based on ^{14}C and $^{33}P_i$ radiotracers, respectively (a). Panel (b) shows the relative contribution (%) of total uptake) of particle size classes to P_i uptake for each station.

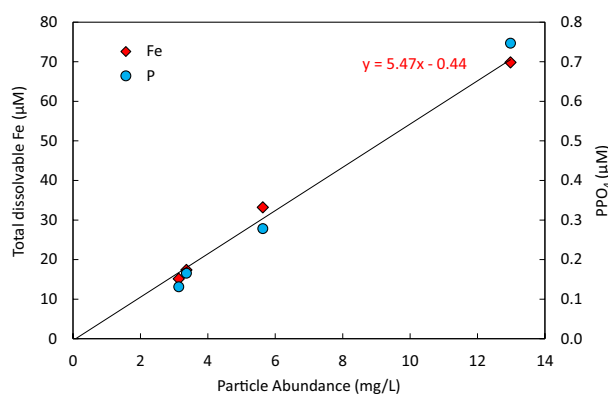


Figure 7. Total dissolvable iron and particulate phosphate data in each of the lava-seawater interaction experiments, plotted against particle abundances (dry weights). Dissolved iron is assumed to be negligible. Particulate phosphate is calculated as the total dissolvable phosphate minus dissolved phosphate. The average Fe/P stoichiometric ratio of the particles is $108 \pm 11\%$ (1σ) and the average abundance of phosphate in the particles is $0.05 \mu\text{mol}/\text{mg} \pm 13\%$ (1σ). The hydration state of the iron oxyhydroxides can be calculated from the slope of the linear fit through the Fe points (as shown); assuming a generalized composition of $\text{FeO}(\text{OH}) \cdot n(\text{H}_2\text{O})$ we find that $n = 5.2$.

that either co-precipitated with the Fe_{ox} or had diffused into the interior of particles (Barrow, 1983; Berner, 1973; Froelich, 1988). Assuming the final distribution of $^{33}P_i$ would follow the partition coefficient reported in Table 2, the rapid exchange in the first 6 h of incubation means that $\sim 33\%$ of the P_i sites were on particle surfaces and should be considered highly labile. Size-fractionated filtration of the 100% incubation indicated that the $^{33}P_i$ distribution was: 0% in particles $<0.6 \mu\text{m}$ diameter; 50% in the $0.6\text{--}2 \mu\text{m}$ range; 41% in the $2\text{--}10 \mu\text{m}$ range; and 9% in particles $>10 \mu\text{m}$.

4. Discussion

4.1. Hydration State of the Fe_{ox}

Of the many Fe_{ox} minerals that occur in nature, the most likely one to have formed in the lava-impacted waters is ferrihydrite. It is generally the first precipitate from an aqueous solution in which Fe supply is rapid and dissolved Si concentrations are above $10 \mu\text{M}$ (Schwertmann & Cornell, 2000), which occurred in our experiments as well as near the ocean entry (Table 2; Figure 5). It is also a common precipitate in mid-ocean ridge hydrothermal plumes (e.g., Feely et al., 1998). Ferrihydrite has inherently poor crystallinity and is sometimes referred to as amorphous Fe_{ox} . It easily incorporates defects and has such a range of hydration states that its specific mineral composition is still a subject of debate (Funnell et al., 2020).

The hydration state of the Fe_{ox} from the quench waters of the synthetic ocean entry experiments can be estimated using the slope of the linear fit through the tdFe points in Figure 7 to define the average molecular weight of the Fe_{ox} . Using the slope of $5.47 (\mu\text{mol Fe}/\text{mg particle})$, and solving for n in the generalized chemical composition of $\text{FeO}(\text{OH}) \cdot n(\text{H}_2\text{O})$, we find that $n = 5.2$. If the formula uses $\text{Fe}_2\text{O}_3 \cdot n(\text{H}_2\text{O})$ (i.e. no structural water) instead, then $n = 11.4$ (with a similar $\text{H}_2\text{O}:\text{Fe}$ ratio of 5.7). These are both upper constraints; if there is substitution of the Fe site with Al (Cornell & Schwertmann, 2003), or any amount of basaltic glass caught on the dry weight filter, the calculated hydration value will be too high. Because the intercept of the fit is near zero, we conclude that the most likely source of uncertainty is assuming that all metal cations are Fe. Al is also a major element of basalt that is abundant in lava-impacted waters (Resing & Sansone, 2002) and can substitute for up to 25% of the Fe sites (Manceau & Gates, 2013). Additionally, Si adsorption onto Fe_{ox} has been documented, but is likely to be $<10\%$ of the Fe concentrations at these micromolar concentrations of dissolved Si (Jones et al., 2015).

4.2. Partitioning of P_i Into Fe_{ox}

In the laboratory, most experiments of P_i adsorption into iron oxides and oxyhydroxides have been performed either on soils and sediments (e.g., Barrow, 1983; Berner, 1973) or particles synthesized at low temperature with purified starting reagents (e.g., Bolan et al., 1985; Jones et al., 2015; Ruttenberg & Sulak, 2011). Natural materials form in chemically complex systems, resulting in unique crystal defects and elemental substitutions that can significantly affect partitioning and sorption/desorption rates (Parfitt, 1989; Strauss et al., 1997; Torrent et al., 1990). Although an attempt to synthesize particles with more natural conditions, as we have done here, will likely lead to a better understanding of a natural

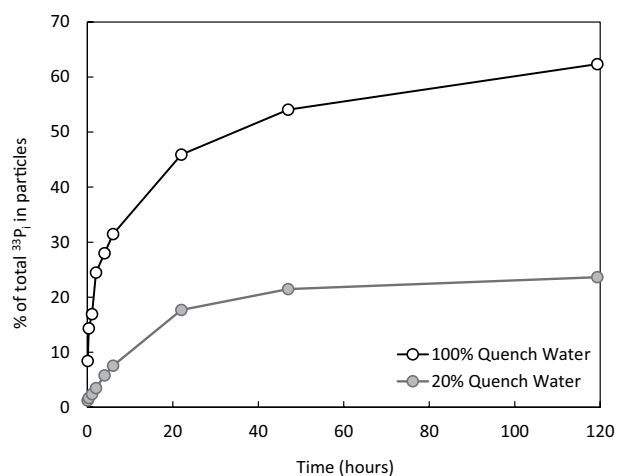


Figure 8. Results of the ³³P_i incubation experiments using quench water from the synthetic ocean entry experiment Beaker A at 100% concentrated and 20% concentrated (diluted 5-fold with surface seawater, SSW). The 20% incubation is corrected for uptake observed in the SSW control.

environment, it introduces a greater number of uncontrolled variables and makes observations more empirical than mechanistically diagnostic.

That being said, one important observation from the synthetic ocean entry experiments is the apparent partitioning of P_i into the Fe_{ox} particles that were generated. Over timescales that are yet to be determined for these particles, the partition coefficient may be complicated by a change in mineralogy from ferrihydrite to the more stable phase of goethite or hematite (Schwertmann & Cornell, 2000), both of which have a lower capacity for P_i (Ruttenberg & Sulak, 2011). Nevertheless, it may be useful to identify a quasi-equilibrium distribution coefficient, K_d, defined as follows:

$$K_d = \frac{\text{concentration of } P_i \text{ in solid } (\mu\text{mol/mg})}{\text{concentration of } P_i \text{ in liquid } (\mu\text{mol/mg})} \quad (1)$$

The log(K_d) for the four quench experiments ranged from 5.8 to 6.2 (Table 2). This compares favorably with data from Feely et al. (1996) on hydrothermal plume particles that were collected above a volcanically active portion of the southern East Pacific Rise. Using the five most particle-rich stations from 16°S to 18.5°S from Feely et al., the average log(K_d)

for the partitioning of P_i into plume particles is 5.7 ± 0.1 (1σ , $n = 31$). Their field particles have a very similar concentration of Fe to our experimental particles, with an average of 5.9 μmol Fe/mg of particle (compared to our ratio of 5.5 μmol/mg; Figure 7), but they have about 20 times higher concentration of P_i, which is reflective of the high concentration of P_i in the ambient deep seawater (2.4 μM).

It is difficult to compare the K_d found in this study to most other experimental studies, in large part because they have evaluated adsorption curves in systems with high particle-to-water ratios and high P loading, with the goal being to measure saturation of P or sorption kinetics, and not equilibrium partitioning of P in a low-particulate and P-undersaturated system. An important exception is the study by Jones et al. (2015) who, expanding on a study by Konhauser et al. (2007), reported P_i partitioning onto synthetic ferrihydrite in seawater and showed that it was strongly dependent on Si concentration (at mM levels). They do not report particle loads (mg/L), only Fe concentrations, so to calculate a K_d as in Equation 1, we assume a conversion factor ranging from 5.5 to 5.9 μmol Fe/mg of particle. Together with our Si concentrations of 39–122 μM, then, the log(K_d) would range from 6.2 to 6.3, which overlap with our estimates.

4.3. Biotic Versus Abiotic Uptake of P_i

The K_d determined through the synthetic ocean entry experiments can be applied to environmental settings in which biological activity is thought to be negligible (i.e., where there is little to no biological demand for P_i). To determine the relative amounts of biotic and abiotic uptake of P_i in the phytoplankton bloom, the ³³P_i radiotracer experiment becomes useful. The incubation with 20% quench water has a Si concentration of 27 μM, which is very similar to the seawater sample from Station 2 that was used to determine P_i uptake (25 μM Si). Although Si is largely a proxy for the amount of rock dissolution (and, hence, Fe_{ox} abundance), it is possible that at least 5 μM of the Si at Station 2 originated from deep water (see next section). Also, the tdFe may be elevated in the experiments due to the steel beakers used, meaning that the Fe_{ox} abundance relative to Si concentrations may have been artificially high compared to the field. For these reasons, the ³³P_i radiotracer experiment using the 20% diluted quench water is not a perfect analogy for Station 2, but it can still be used to provide an upper constraint on abiotic P_i uptake. Correcting the Station 2 uptake with the uptake rate from the 20% diluted quench water over the first 6 h, the remaining, biological uptake equates to 35 nM/day (50% of the original rate) and the resulting C:P uptake ratio for Station 2 is 104:1, which is much more reasonable for the observed community composition than the original ratio of 45:1 and more similar to the other field stations (Figure 6).

4.4. Mass Balance Considerations for Field Data

Because the background seawater offshore of Kilauea contains Fe at nanomolar concentrations (Boyle et al., 2005), and basalt contains 11 wt% FeO, we can assume that all elevated concentrations of Fe in the lava-impacted seawater derives from rock dissolution. And because mantle-derived, basaltic melts contain no appreciable fixed N (Fischer & Chiodini, 2015), we can assume that all excess N + N in seawater samples derives from the thermal upwelling of deep, nutrient-rich seawater. Although thermal fixation of atmospheric dinitrogen can occur at the surface of lava flows (Huebert et al., 1999; Mather et al., 2004), it is not believed to be a contributor to the elevated marine N + N because the prevailing wind directions during the 2018 eruption advected lava gases, vapors, and laze onshore rather than out to sea and also because the isotopic composition of the N + N is inconsistent with that process (Wilson et al., 2019).

Because Si and P_i occur in significant concentrations in both basalt and deep seawater, their relationships with tdFe and N + N are important for understanding the relative contribution of each source to the phytoplankton bloom. Si and tdFe of field samples are tightly correlated (Figure 5a) with a slope that falls very close to the projected mixing line for basalt dissolution into seawater (using the lava composition in Table 1). The maximum tdFe values found represent the dissolution of 1 mg basalt per L seawater (1 ppm). An overall shift to higher Si concentrations reflects a component of deep water that amounts to increases of 3–4 μM Si for these tow-fish samples. Assuming that the correlation with tdFe holds for the station profiles and near-shore underway samples, the highest Si concentrations observed (36 μM ; Figure 5c) represent ~ 3 mg/L rock dissolution.

N + N concentrations constrain the proportion of deep seawater. Wilson et al. (2019) used nitrogen and oxygen isotopic data to infer that the deep water originated from a depth of ~ 300 m. Based on well-established nutrient profiles for the surrounding oligotrophic ocean (Karl et al., 2001, with additional data available at <https://hahana.soest.hawaii.edu/hot/>), 300 m deep seawater contains 10 μM N + N. Therefore the maximum observed value of 4.7 μM from Station 2 means that up to 47% of the water mass is from thermal upwelling. As water deepens past 300 m, N + N concentrations continue to increase and, hence, it takes a smaller percentage of deeper water to form the observed concentrations in the lava-impacted plume: a minimum of 11% water would be needed with water originating from $\geq 1,000$ m and containing 42 μM N + N (Karl et al., 2001). The ratio of Si:(N + N) is 1:1 at 300 m, 2:1 at 600 m and 2.6:1 at 1,000 m; therefore, 5–12 μM Si could be delivered by deep water into the parcel of surface water containing the 4.7 μM N + N.

The lava-impacted waters are obviously not well mixed, as noted earlier for the chlorophyll concentrations and particle counts (Figure 2). Even at Station 2, there are very different nutrient concentrations within 20 m of depth (see Figure 5b for the range within the upper 45 m), which are likely the result of hydrovolcanic explosions, pulses of lava addition, and thermal equilibration. One thing that remains a constant throughout all the near-shore samples is a depletion in P_i . Using the plot of Si versus P_i in Figure 5c, we can algebraically remove the rock component and compare the resulting deep-water component to that predicted by the (N + N) data. For example, taking the total P content (dissolved plus particulate) from the highest (N + N) sample of Station 2 and projecting back along the rock slope results in an interception of the deep-water mixing line at 0.23 μM P_i (Figure 5c)—a 40% deficit from the predicted P_i (0.38 μM , assuming 47% of water from 300 m, which contains 0.75 μM P_i). Ultimately, there is no combination of rock plus deep water mixing that results in a mass balance for P_i in the high N + N Station 2 samples. Deficits in P_i only increase if we use deeper water with higher nutrient concentrations.

From the tow-fish data, we can independently calculate expected P_i in another way using the tdFe data to estimate the rock contribution and N + N to calculate the deep-water contribution. The rock ratio is set at a molar Fe/P ratio of 41.6 (Table 1), and deep water has a (N + N)/ P_i ratio of 14 ± 1 over all applicable depths (Karl et al., 2001). Expected values of P_i are plotted with observed P_i concentrations in Figure 9, assuming the rock and deep-water components are added to a background P_i concentration of 0.09 μM for surface seawater. The model predictions show a 2-fold increase in P_i after Station 4 (coincident with the highest tdFe and (N + N), as seen in Figure 4), which is clearly missing in the observed values. The differences (up to 0.1 μM) are not expected to be in the Fe_{ox} fraction, which we estimate to contain ≤ 0.015 μM P_i (taking the maximum tdFe of 1.4 μM , converting to particle load using 5.5 μmol Fe/mg, and applying the observations from Station 2 showing PPO_4 concentrations of 0.05 μmol P/mg). Any extra particulate organic matter in

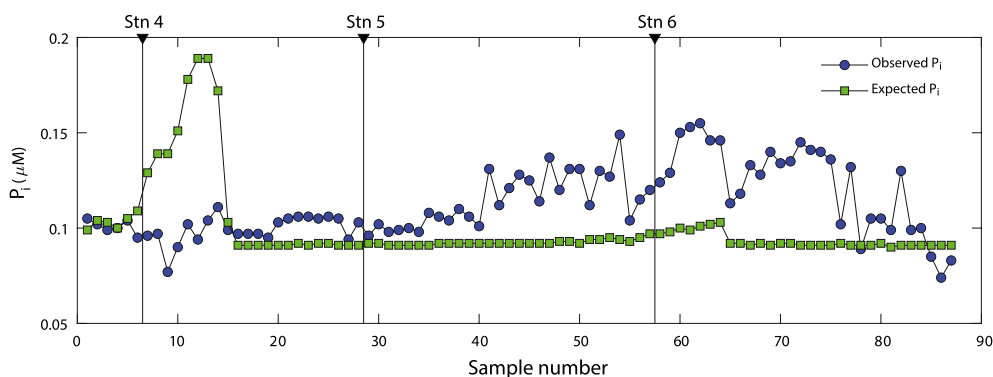


Figure 9. Observed concentrations of P_i from the tow-fish sampler plotted in sampling order along cruise track. Expected concentrations of P_i in these surface waters are calculated from measured $tdFe$ and $N + N$ concentrations, assuming $tdFe$ represents a rock component and $N + N$ represents a deep seawater component. Model results shown use a Fe/P molar ratio of 43.1 for Vent 8 basalt (Table 1) and a deep seawater $(N + N)/P_i$ ratio of 14 (Karl et al., 2001). Calculated rock and deepwater components are added to a background P_i concentration of $0.09 \mu M$.

this region would take up $N + N$ and P_i in nearly the same proportion as they occur in deep water, meaning that the consideration of organic matter does not change the estimates for missing P_i . Overall, the near-shore P_i deficit is an unresolved issue, but hypotheses for loss include: (a) settling of particles; (b) scavenging of P_i as deep water was upwelled along lava fronts and across volcanoclastic sediments; (c) presence of some dissolved P as compounds that were not detected (such as polyphosphate); and (d) particulate P that was not fully recovered in our analysis.

From Station 5 and beyond, there is a shift from a P_i deficit to a broad peak of excess P_i , up to $0.07 \mu M$. It is possible that this pattern is displaying natural background conditions and has nothing to do with lava input. However, an alternative hypothesis is that P_i desorbed from Fe_{ox} particles as the particles left the lava-impacted, near-shore zone and entered waters that had a lower total budget of P_i , which would promote desorption according to the principles of equilibrium elemental partitioning (Equation 1). Assuming a flow rate of 0.4 m/sec (Wilson et al., 2019), the water parcel at Station 4 would have taken 0.3 days to arrive from the lava ocean entry, and for Stations 5 and 6, it would have taken 1.6 and 3 days, respectively. Because of the heterogenous nature of the lava-impacted waters, it is very difficult to say what a given parcel of water looked like when it was near shore or what its biogeochemical history might have been. Theoretically, from the $^{33}P_i$ radiotracer results, the transit times were long enough for significant re-equilibration to occur for the highly labile surface sites (estimated to be $\sim 1/3$ of the total P_i sites; Section 3.4). It is likely that some portion of the more tightly (or, possibly, irreversibly) bound P_i could not desorb on any relevant time scales (Barrow, 1983; Ruttenberg & Sulak, 2011). A caveat to this hypothesis is that particulate matter must have been settling out of the water column as the P_i was desorbing since $tdFe$ concentrations were low.

5. Conclusions

The most relevant information provided by this work is not about the magnitude of the event studied. Both the eruption volume (0.8 km^3 ; Neal et al., 2019) and the extent of the phytoplankton bloom (Figure 1) are small on a global scale. Rather, this study describes an important dynamic process that happens on a much larger scale in locations and times that are difficult (or even impossible) to access. For example, Bjerrum and Canfield (2002) hypothesized that 3.2 to 1.9 billion years ago, during the widespread deposition of banded iron formations, extensive co-precipitation of P_i with Fe_{ox} stripped the oceans of most of their P_i inventory, which imposed severe P_i limitation on photosynthesis and, consequentially, caused sluggish oxygenation of the atmosphere. The formation of large igneous provinces in the ocean (oceanic plateaus) may also have been a setting in which similar processes would have impacted the biogeochemistry of the surface oceans over significant time and length scales (Courtillot & Renne, 2003).

With respect to the modern ocean, there is a widespread belief that marine primary production throughout much of the globe is limited by fixed nitrogen (Moore et al., 2013). However, a strong case can be made

that nitrogen fixation by diazotrophs—which can provide fixed nitrogen to other microorganisms—is often limited by Fe and P_i (Letelier et al., 2019; Sohm et al., 2011). This means that a low abundance of fixed N only happens because of an underlying depletion of Fe and/or P_i . Volcanic fertilization of the euphotic zone through either atmospheric dust/ash deposition or lava-seawater interaction has the potential to alleviate this underlying nutrient limitation in oligotrophic waters. However, the scavenging of dissolved P_i by Fe_{ox} precipitates could create transient depletion events on a local scale, especially near the coast. On the other hand, our new data also suggests that further away from the intense source of volcanic input, P_i can desorb from Fe_{ox} , thereby providing a far-field supply of dissolved P_i .

Previous studies have detected patches of increased chlorophyll by satellite offshore of Japan after the eruption of Miyake-jima volcano (Uematsu et al., 2004), in the NE Pacific following the eruption of Kasatochi volcano (Hamme et al., 2010; Langmann et al., 2010), and in the western Pacific following an eruption in the Mariana Islands (Lin et al., 2011). In general, Fe from volcanic fallout is viewed as the main driver of enhanced primary productivity (Duggen et al., 2010), but field sampling is too sparse to fully describe the overall nutrient dynamics in those perturbed environments. In addition, very little attention has been given to the role of P_i within the topic of volcanic fertilization. One huge unknown is whether or not P_i and Fe that are contained in Fe_{ox} particles are bioavailable to microorganisms. This is an important avenue of future investigations, as it is a factor in most modes of volcanic fertilization—from ash fallout, to lava-seawater interaction and submarine volcanism—as well as being relevant to the biological impact of particles derived from continental weathering and dust input.

The dominant sink of modern marine P occurs through sedimentation and burial of both organic and inorganic compounds. The deposition of Fe_{ox} (containing scavenged P) accounts for 15%–54% of the total P flux out of the oceans and into open ocean marine sediments (Benitez-Nelson, 2000; Paytan & McLaughlin, 2007; Ruttenger, 1993). With a warming climate, greater continental weathering is predicted (Berner et al., 1983) and would result in enhanced delivery of Fe_{ox} to the marine environment. In seawater, the average dissolved P_i concentration is $\sim 2 \mu M$ (World Ocean Atlas) and the average Fe is $< 1 \text{ nM}$ (Boyd & Ellwood, 2010), so the P_i/Fe ratio is > 2000 . Terrigenous sediments are Fe-rich and have a P/Fe ratio that is likely < 0.1 (Plank & Langmuir, 1998), so increasing the continental flux to the oceans has the potential to change the average concentration of dissolved P_i by introducing large quantities of Fe that could scavenge P_i from the water column. Increased delivery of Fe_{ox} into the euphotic zone could be especially detrimental to primary productivity in oligotrophic settings in which the P_i concentrations are already low.

Data Availability Statement

New nutrient and particulate data presented here can be found as supplementary information to this article as well as at the following data repository site: <https://doi.org/10.5281/zenodo.4574201>. Previously published data on Fe, some nutrients and chlorophyll concentrations can be found in Hawco et al. (2020; <https://doi.org/10.1016/j.gca.2020.05.005>) and Wilson et al. (2019; <https://doi.org/10.1126/science.aax4767>).

References

- Achterberg, E. P., Moore, C. M., Henson, S. A., Steigenberger, S., Stohl, A., Eckhardt, S., et al. (2013). Natural iron fertilization by the Eyjafjallajökull volcanic eruption. *Geophysical Research Letters*, *40*, 921–926. <https://doi.org/10.1002/grl.50221>
- Barrow, N. J. (1983). A mechanistic model for describing the sorption and desorption of phosphate by soil. *Journal of Soil Science*, *34*, 733–750. <https://doi.org/10.1111/j.1365-2389.1983.tb01068.x>
- Benitez-Nelson, C. R. (2000). The biogeochemical cycling of phosphorus in marine systems. *Earth-Science Reviews*, *51*, 109–135. [https://doi.org/10.1016/S0012-8252\(00\)00018-0](https://doi.org/10.1016/S0012-8252(00)00018-0)
- Berner, R. A. (1973). Phosphate removal from sea water by adsorption on volcanogenic ferric oxides. *Earth and Planetary Science Letters*, *18*, 77–86. [https://doi.org/10.1016/0012-821x\(73\)90037-x](https://doi.org/10.1016/0012-821x(73)90037-x)
- Berner, R. A., Lasaga, A. C., & Garrels, R. M. (1983). The carbonate-silicate geochemical cycle and its effect on atmospheric carbon dioxide over the past 100 million years. *American Journal of Science*, *283*, 641–683. <https://doi.org/10.2475/ajs.283.7.641>
- Bjerrum, C. J., & Canfield, D. E. (2002). Ocean productivity before about 1.9 Gyr ago limited by phosphorus adsorption onto iron oxides. *Nature*, *417*, 159–162. <https://doi.org/10.1038/417159a>
- Björkman, K. M., Duhamel, S., Church, M. J., & Karl, D. M. (2018). Spatial and temporal dynamics of inorganic phosphate and adenosine-5'-triphosphate in the North Pacific Ocean. *Frontiers in Marine Science*, *5*, 235. <https://doi.org/10.3389/fmars.2018.00235>
- Björkman, K. M., Duhamel, S., & Karl, D. M. (2012). Microbial group specific uptake kinetics of inorganic phosphate and adenosine-5-triphosphate (ATP) in the North Pacific Subtropical Gyre. *Frontiers in Microbiology*, *3*, 189. <https://doi.org/10.3389/fmicb.2012.00189>

Acknowledgments

This work was supported by grants from the Simons Foundation (329108, D. M. K.; and 602538, N. J. H.), the Gordon and Betty Moore Foundation (3794, D. M. K.), the Balzan Prize for Oceanography (D. M. K.), and the National Science Foundation (OCE-1842012, D. M. K.). The authors especially thank Linda Yamamoto for turning the metal casting studio of UHM Art Department into a science lab, Mike Garcia for guidance on rock collection on Mauna Loa, Scott Roland for his participation in the lava quench experiments, Lance Fujieki for graphics assistance, Ryan Tabata for photography, Kendra Babcock for the analysis of particulate Si, and the captain and crew of the *R/V Ka'imika'i-O-Kanaloa*. The authors are also grateful for valuable scientific input on this paper from Frank Sansone, Tobias Fischer, and Stanley Hart, in addition to helpful reviews by Philip Froelich, and one other anonymous reviewer.

- Bolan, N. S., Barrow, N. J., & Posner, A. M. (1985). Describing the effect of time on sorption of phosphate by iron and aluminum hydroxides. *Journal of Soil Science*, 36, 187–197. <https://doi.org/10.1111/j.1365-2389.1985.tb00323.x>
- Boyd, P. W., & Ellwood, M. J. (2010). The biogeochemical cycle of iron in the ocean. *Nature Geoscience*, 3, 675–682. <https://doi.org/10.1038/ngeo964>
- Boyle, E. A., Bergquist, B. A., Kayser, R. A., & Mahowald, N. (2005). Iron, manganese, and lead at Hawaii Ocean Time-series station ALOHA: Temporal variability and an intermediate water hydrothermal plume. *Geochimica et Cosmochimica Acta*, 69, 933–5166. <https://doi.org/10.1016/j.gca.2005.03.006>
- Cornell, R. M., & Schwertmann, U. (2003). *The iron oxides: Structure, properties, reactions, occurrences, and uses* (p. 664). New York, NY and Weinheim: Wiley-VCH.
- Courtillot, V. E., & Renne, P. R. (2003). On the ages of flood basalt events. *Comptes Rendus Geoscience*, 335, 113–140. [https://doi.org/10.1016/S1631-0713\(03\)00006-3](https://doi.org/10.1016/S1631-0713(03)00006-3)
- DeMaster, D. J. (1981). The supply and accumulation of silica in the marine environment. *Geochimica et Cosmochimica Acta*, 45, 1715–1732. [https://doi.org/10.1016/0016-7037\(81\)90006-5](https://doi.org/10.1016/0016-7037(81)90006-5)
- Dore, J. E., Houlihan, T., Hebel, D. V., Tien, G., Tupas, L., & Karl, D. M. (1996). Freezing as a method of sample preservation for the analysis of dissolved inorganic nutrients in seawater. *Marine Chemistry*, 53, 173–185. [https://doi.org/10.1016/0304-4203\(96\)00004-7](https://doi.org/10.1016/0304-4203(96)00004-7)
- Duggen, S., Olgun, N., Croot, P., Hoffmann, L., Dietze, H., Delmelle, P., & Teschner, C. (2010). The role of airborne volcanic ash for the surface ocean biogeochemical iron-cycle: A review. *Biogeosciences*, 7, 827–844. <https://doi.org/10.5194/bg-7-827-2010>
- Feely, R. A., Baker, E. T., Marumo, K., Urabe, T., Ishibashi, J., Gendron, J., et al. (1996). Hydrothermal plume particles and dissolved phosphate over the superfast-spreading southern East Pacific Rise. *Geochimica et Cosmochimica Acta*, 60, 2297–2323. [https://doi.org/10.1016/0016-7037\(96\)00099-3](https://doi.org/10.1016/0016-7037(96)00099-3)
- Feely, R. A., Trefry, J. H., Lebon, G. T., & German, C. R. (1998). The relationship between P/Fe and V/Fe ratios in hydrothermal precipitates and dissolved phosphate in seawater. *Geophysical Research Letters*, 25, 2253–2256. <https://doi.org/10.1029/98gl01546>
- Fischer, T. P., & Chiodini, G. (2015). Volcanic, magmatic and hydrothermal gases. In H. Sigurdsson, B. Houghton, H. Rymer, J. Stix, & S. McNutt (Eds.), *The encyclopedia of volcanoes* (2nd ed., pp. 779–797). Academic Press. <https://doi.org/10.1016/B978-0-12-385938-9.00045-6>
- Foreman, R. K., Segura-Noguera, M., & Karl, D. M. (2016). Validation of Ti(III) as a reducing agent in the chemiluminescent determination of nitrate and nitrite in seawater. *Marine Chemistry*, 186, 83–89. <https://doi.org/10.1016/j.marchem.2016.08.003>
- Froelich, P. N. (1988). Kinetic control of dissolved phosphate in natural rivers and estuaries: A primer on the phosphate buffer mechanism. *Limnology & Oceanography*, 33, 649–668. <https://doi.org/10.4319/lo.1988.33.4part2.0649>
- Funnell, N. P., Fulford, M. F., Inoue, S., Kletetschka, K., Michel, F. M., & Goodwin, A. L. (2020). Nanocomposite structure of two-line ferrihydrite powder from total scattering. *Communications Chemistry*, 3, 22. <https://doi.org/10.1038/s42004-020-0269-2>
- Gansecki, C., Lee, R. L., Shea, T., Lundblad, S. P., Hon, K., & Parcheta, C. (2019). The tangled tale of Kilauea's 2018 eruption as told by geochemical monitoring. *Science*, 366, eaaz0147. <https://doi.org/10.1126/science.aaz0147>
- González, A. G., Santana-Casiano, J. M., Pérez, N., & González-Dávila, M. (2010). Oxidation of Fe(II) in natural waters at high nutrient concentrations. *Environmental Science & Technology*, 44, 8095–8101. <https://doi.org/10.1021/es1009218>
- González-Vega, A., Fraile-Nuez, E., Santana-Casiano, J. M., González-Dávila, M., Escánez-Pérez, J., Gómez-Ballesteros, M., et al. (2020). Significant release of dissolved inorganic nutrients from the shallow submarine volcano Tagoro (Canary Islands) based on seven-year monitoring. *Frontiers in Marine Science*, 6. <https://doi.org/10.3389/fmars.2019.00829>
- Hamme, R. C., Webley, P. W., Crawford, W. R., Whitney, F. A., DeGrandpre, M. D., Emerson, S. R., et al. (2010). Volcanic ash fuels anomalous plankton bloom in subarctic northeast Pacific. *Geophysical Research Letters*, 37, L19604. <https://doi.org/10.1029/2010GL044629>
- Hawco, N. J., Yang, S.-C., Foreman, R. K., Funkey, C. P., Dugenne, M., White, A. E., et al. (2020). Metal isotope signatures from lava-seawater interaction during the 2018 eruption of Kilauea. *Geochimica et Cosmochimica Acta*, 282, 340–356. <https://doi.org/10.1016/j.gca.2020.05.005>
- Holmes, R. M., Aminot, A., Krouel, R., Hooker, B. A., & Peterson, B. J. (1999). A simple and precise method for measuring ammonium in marine and freshwater ecosystems. *Canadian Journal of Fisheries and Aquatic Sciences*, 56, 1801–1808. <https://doi.org/10.1139/cjfas-56-10-1801>
- Huebert, B., Vitousek, P., Sutton, J., Elias, T., Heath, J., Coeppicus, S., et al. (1999). Volcano fixes nitrogen into plant-available forms. *Biogeochemistry*, 47, 111–118. <https://doi.org/10.1007/bf00993099>
- Huntley, M. E., Johnson, Z. I., Brown, S. L., Sills, D. L., Gerber, L., Archibald, I., et al. (2015). Demonstrated large-scale production of marine microalgae for fuels and feed. *Algal Research*, 10, 249–265. <https://doi.org/10.1016/j.algal.2015.04.016>
- Jones, C., Nomosatryo, S., Crowe, S. A., Bjerrum, C. J., & Canfield, D. E. (2015). Iron oxides, divalent cations, silica, and the early earth phosphorus crisis. *Geology*, 43, 135–138. <https://doi.org/10.1130/G36044.1>
- Karl, D. M. (2002). Nutrient dynamics in the deep blue sea. *Trends in Microbiology*, 10, 410–418. [https://doi.org/10.1016/S0966-842X\(02\)02430-7](https://doi.org/10.1016/S0966-842X(02)02430-7)
- Karl, D. M., Björkman, K. M., Dore, J. E., Fujieki, L., Hebel, D. V., Houlihan, T., et al. (2001). Ecological nitrogen-to-phosphorus stoichiometry at station ALOHA. *Deep-Sea Research Part II*, 48, 1529–1566. [https://doi.org/10.1016/s0967-0645\(00\)00152-1](https://doi.org/10.1016/s0967-0645(00)00152-1)
- Karl, D. M., & Lukas, R. (1996). The Hawaii Ocean Time-series (HOT) program: Background, rationale and field implementation. *Deep-Sea Research Part II*, 43, 129–156. [https://doi.org/10.1016/0967-0645\(96\)00005-7](https://doi.org/10.1016/0967-0645(96)00005-7)
- Karl, D. M., McMurtry, G. M., Malahoff, A., & Garcia, M. O. (1988). Loihi Seamount, Hawaii: A mid-plate volcano with a distinctive hydrothermal system. *Nature*, 335, 532–535. <https://doi.org/10.1038/335532a0>
- Konhauser, K. O., Lalonde, S. V., Amskold, L., & Holland, H. D. (2007). Was there really an Archean phosphate crisis? *Science*, 315, 1234. <https://doi.org/10.1126/science.1136328>
- Koroleff, F. (1983). Determination of silicon. In K. Grasshoff, M. Ehrhardt, & K. Kremling (Eds.), *Methods of seawater analysis*, (2nd ed., pp. 174–187). Weinheim, Germany: Verlag Chemie.
- Langmann, B., Zakšek, K., Hort, M., & Duggen, S. (2010). Volcanic ash as fertiliser for the surface ocean. *Atmospheric Chemistry and Physics*, 10, 3891–3899. <https://doi.org/10.5194/acp-10-3891-2010>
- Letelier, R. M., Björkman, K. M., Church, M. J., Hamilton, D. S., Mahowald, N. M., Scanza, R. A., et al. (2019). Climate-driven oscillation of phosphorus and iron limitation in the North Pacific Subtropical Gyre. *Proceedings of the National Academy of Sciences*, 116, 12720–12728. <https://doi.org/10.1073/pnas.1900789116>
- Lin, I. I., Hu, C., Li, Y. H., Ho, T.-Y., Fischer, T. P., Wong, G. T. F., et al. (2011). Fertilization potential of volcanic dust in the low-nutrient low-chlorophyll western North Pacific subtropical gyre: Satellite evidence and laboratory study. *Global Biogeochemical Cycles*, 25, GB1006. <https://doi.org/10.1029/2009GB003758>

- Manceau, A., & Gates, W. P. (2013). Incorporation of Al in iron oxyhydroxides: Implications for the structure of ferrihydrite. *Clay Minerals*, 48, 481–489. <https://doi.org/10.1180/claymin.2013.048.3.05>
- Mather, T. A., Allen, A. G., Davison, B. M., Pyle, D. M., Oppenheimer, C., & McGonigle, A. J. S. (2004). Nitric acid from volcanoes. *Earth and Planetary Science Letters*, 218, 17–30. [https://doi.org/10.1016/S0012-821X\(03\)00640-X](https://doi.org/10.1016/S0012-821X(03)00640-X)
- Mattox, T. N., & Mangan, M. T. (1997). Littoral hydrovolcanic explosions: A case study of lava-seawater interaction at Kilauea Volcano. *Journal of Volcanology and Geothermal Research*, 75, 1–17. [https://doi.org/10.1016/S0377-0273\(96\)00048-0](https://doi.org/10.1016/S0377-0273(96)00048-0)
- Moore, C. M., Mills, M. M., Arrigo, K. R., Berman-Frank, I., Bopp, L., Boyd, P. W., et al. (2013). Processes and patterns of oceanic nutrient limitation. *Nature Geoscience*, 6, 701–710. <https://doi.org/10.1038/ngeo1765>
- Murphy, J., & Riley, J. P. (1962). A modified single solution method for the determination of phosphate in natural waters. *Analytica Chimica Acta*, 27, 31–36. [https://doi.org/10.1016/S0003-2670\(00\)88444-5](https://doi.org/10.1016/S0003-2670(00)88444-5)
- Neal, C. A., Brantley, S. R., Antolik, L., Babb, J. L., Burgess, M., Calles, K., et al. (2019). The 2018 rift eruption and summit collapse of Kilauea Volcano. *Science*, 363, 367–374. <https://doi.org/10.1126/science.aav7046>
- Parfitt, R. L. (1989). Phosphate reactions with natural allophane, ferrihydrite and goethite. *Journal of Soil Science*, 40, 359–369. <https://doi.org/10.1111/j.1365-2389.1989.tb01280.x>
- Paytan, A., & McLaughlin, K. (2007). The oceanic phosphorus cycle. *Chemical Reviews*, 107, 563–576. <https://doi.org/10.1021/cr0503613>
- Plank, T., & Langmuir, C. H. (1998). The chemical composition of subducting sediment and its consequences for the crust and mantle. *Chemical Geology*, 145, 325–394. [https://doi.org/10.1016/S0009-2541\(97\)00150-2](https://doi.org/10.1016/S0009-2541(97)00150-2)
- Resing, J. A., & Sansone, F. J. (2002). The chemistry of lava-seawater interactions II: The elemental signature. *Geochimica et Cosmochimica Acta*, 66, 1925–1941. [https://doi.org/10.1016/S0016-7037\(01\)00897-3](https://doi.org/10.1016/S0016-7037(01)00897-3)
- Ruttenberg, K. C. (1993). Reassessment of the oceanic residence time of phosphorus. *Chemical Geology*, 107, 405–409. [https://doi.org/10.1016/0009-2541\(93\)90220-d](https://doi.org/10.1016/0009-2541(93)90220-d)
- Ruttenberg, K. C., & Sulak, D. J. (2011). Sorption and desorption of dissolved organic phosphorus onto iron (oxyhydr)oxides in seawater. *Geochimica et Cosmochimica Acta*, 75, 4095–4112. <https://doi.org/10.1016/j.gca.2010.10.033>
- Sansone, F. J., & Smith, J. R. (2006). Rapid mass wasting following nearshore submarine volcanism on Kilauea volcano, Hawaii. *Journal of Volcanology and Geothermal Research*, 151, 133–139. <https://doi.org/10.1016/j.jvolgeores.2005.07.026>
- Santana-González, C., Santana-Casiano, J. M., González-Dávila, M., & Fraile-Nuez, E. (2017). Emissions of Fe(II) and its kinetic oxidation at Togoro submarine volcano, El Hierro. *Marine Chemistry*, 195, 129–137. <https://doi.org/10.1016/j.marchem.2017.02.001>
- Schwertmann, U., & Cornell, R. M. (2000). *Iron oxides in the laboratory: Preparation and characterization* (p. 188). Weinheim and New York, NY: Wiley-VCH.
- Sohm, J. A., Webb, E. A., & Capone, D. G. (2011). Emerging patterns of marine nitrogen fixation. *Nature Reviews Microbiology*, 9, 499–508. <https://doi.org/10.1038/nrmicro2594>
- Soule, S. A., Zoeller, M., & Parcheta, C. (2021). Submarine lava deltas of the 2018 eruption of Kilauea volcano. *Bulletin of Volcanology*, 83, 23. <https://doi.org/10.1007/s00445-020-01424-1>
- Strauss, R., Brümmer, G. W., & Barrow, N. J. (1997). Effects of crystallinity of goethite: II. Rates of sorption and desorption of phosphate. *European Journal of Soil Science*, 48, 101–114. <https://doi.org/10.1111/j.1365-2389.1997.tb00189.x>
- Strickland, J. D. H., & Parsons, T. R. (1972). *A practical handbook of seawater analysis fisheries* (2nd ed., Vol. 157, p. 310). Ottawa: Research Board of Canada.
- Torrent, J., Barrón, V., & Schwertmann, U. (1990). Phosphate adsorption and desorption by goethites differing in crystal morphology. *Soil Science Society of America Journal*, 54, 1007–1012. <https://doi.org/10.2136/sssaj1990.03615995005400040012x>
- Tyrrell, T. (1999). The relative influences of nitrogen and phosphorus on oceanic primary production. *Nature*, 400, 525–531. <https://doi.org/10.1038/22941>
- Uematsu, M., Toratani, M., Kajino, M., Narita, Y., Senga, Y., & Kimoto, T. (2004). Enhancement of primary productivity in the western North Pacific caused by the eruption of the Miyake-Jima Volcano. *Geophysical Research Letters*, 31. <https://doi.org/10.1029/2003GL018790>
- White, A. E., Letelier, R. M., Whitmire, A. L., Barone, B., Bidigare, R. R., Church, M. J., & Karl, D. M. (2015). Phenology of particle size distributions and primary productivity in the North Pacific subtropical gyre (Station ALOHA). *Journal of Geophysical Research: Oceans*, 120, 7381–7399. <https://doi.org/10.1002/2015JC010897>
- Wilson, S., Hawco, N. J., Armbrust, E. V., Barone, B., Björkman, K. M., Boysen, A. K., et al. (2019). Kilauea lava fuels phytoplankton bloom in the North Pacific Ocean. *Science*, 365, 1040–1044. <https://doi.org/10.1126/science.aax4767>
- Yamagata, Y., Watanabe, H., Saitoh, M., & Namba, T. (1991). Volcanic production of polyphosphates and its relevance to prebiotic evolution. *Nature*, 352, 516–519. <https://doi.org/10.1038/352516a0>